



Probabilistic modeling of dam failure scenarios: a case study of Kanlikoy Dam in Cyprus

A. O. Turkel¹ · Hasan Zaifoglu² · A. M. Yanmaz¹

Received: 18 May 2023 / Accepted: 31 March 2024 / Published online: 17 April 2024
© The Author(s) 2024

Abstract

One of the most perilous natural hazards is flooding resulting from dam failure, which can devastate downstream infrastructure and lead to significant human casualties. In recent years, the frequency of flash floods in the northern part of Nicosia, Cyprus, has increased. This area faces increased risk as it lies downstream of the Kanlikoy Dam, an aging earth-fill dam constructed over 70 years ago. In this study, we aim to assess potential flood hazards stemming from three distinct failure scenarios: piping, 100-year rainfall, and probable maximum precipitation (PMP). To achieve this, HEC-HMS hydrologic model findings were integrated into 2D HEC-RAS hydraulic models to simulate flood hydrographs and generate flood inundation and hazard maps. For each scenario, Monte Carlo simulations using McBreach software produced four hydrographs corresponding to exceedance probabilities of 90%, 50%, 10%, and 1%. The results indicate that all dam breach scenarios pose a significant threat to agricultural and residential areas, leading to the destruction of numerous buildings, roads, and infrastructures. Particularly, Scenario 3, which includes PMP, was identified as the most destructive, resulting in prevailing flood hazard levels of H5 and H6 in the inundated areas. The proportion of inundated areas in these high hazard levels varied between 52.8% and 57.4%, with the number of vulnerable structures increasing from 248 to 321 for exceedance probabilities of 90% and 1%, respectively. Additionally, the number of flooded buildings ranged from 842 to 935, and 26 to 34 km of roads were found to be inundated in this scenario. These findings revealed the need for authorities to develop comprehensive evacuation plans and establish an efficient warning system to mitigate the flood risks associated with dam failure.

Keywords Dam failure · Kanlikoy Dam · Monte Carlo · 2D HEC-RAS · Flood hazard

✉ Hasan Zaifoglu
zhasan@metu.edu.tr

A. O. Turkel
onat.turkel@metu.edu.tr

A. M. Yanmaz
myanz@metu.edu.tr

¹ Department of Civil Engineering, Middle East Technical University, Ankara, Turkey

² Civil Engineering Program, Middle East Technical University, Northern Cyprus Campus, Guzelyurt via Mersin 10, 99738 Kalkanli, Turkey

1 Introduction

Dams are hydraulic structures designed to retain water for the purpose of flow regulation and control. They serve as valuable infrastructure, providing various benefits, such as hydroelectric power generation, agricultural irrigation, flood mitigation, and water storage for both domestic and industrial purposes. Due to their potential for failure, every dam poses a certain level of risk and this event could be resulted in devastating floods downstream. These rare failures occur suddenly, and they can cause both structural damage and loss of lives mostly more than regular flood events due to releasing of a vast amount of water with high discharge in a short amount of time. For instance, the Teton Dam, a 93-m-high rock fill dam located in the United States, collapsed in 1976 due to piping shortly after its initial reservoir filling. This catastrophic event resulted in the loss of ten lives, injured 2000 people, and caused damage to over 7000 properties (Solava and Delatte 2003). Similarly, in Spain, the rockfill dam of Tous failed during a heavy storm in 1982, causing the inundation of 300 square kilometers of inhabited land and towns, and affecting approximately 200,000 people (Alcrudo and Mulet 2007). More recently, the Association of Dam Safety Officials (ASDSO 2023) database has documented over 350 dam failures in United States between January 2000 and November 2022. Particularly, in the context of climate change and its impact on extreme precipitation events, the development of a contingency plan for dam failures, along with preemptive measures to mitigate the negative consequences of a potential catastrophic incident, is of paramount importance.

The primary reasons for dam failure include piping, overtopping, and some structural problems (Wahl 1998). In addition, earthquakes, slope stability, and sabotage incidents are other contributing factors that can lead to overtopping and piping. Overtopping failure may occur when the spillway capacity is insufficient or when a severe flood exceeds design limits (Brunner 2014) due to factors such as increased nonpermeable surfaces with urbanization, deforestation, and more frequent and intense extreme climatic events resulting from climate change. The flow over the embankment generates tractive shear stress on the crest surface and initiates erosion at a vulnerable point. Moreover, piping is a form of dam failure that occurs when internal erosion causes soil particles to be gradually carried away by seeping water, leading to the formation of a pipe in the downstream slope as more material is removed, thereby accelerating the erosion process (Zhang et al. 2016). Typically, a concrete dam is susceptible to sudden failure when the entire structure or a portion of it loses stability under specific loading conditions, such as seismic loading. Conversely, an earth-fill dam is prone to gradual failure due to the erosion of its materials caused by water flow or wave actions, particularly in mixed-regime flows (ASCE/EWRI Task Committee on Dam/Levee Breaching 2011). In this process, as the reservoir's water level falls, the dam breach outflow discharge rises to a peak as the breach widens until it finds equilibrium. Unlike concrete dams, determining the characteristics of a breach in earth-fill dams is challenging and demanding as it requires predicting the complex interactions between soil, water, and structure. These characteristics of the final breach can be summarized by the width, shape, side slopes, maximum flow, and time of failure. According to Froehlich (2008), the formation of a breach in an earth-fill dam is influenced by various factors, such as geometry, material composition, construction techniques, type and extent of protective cover on the crest and slope, size of the reservoir, inflow during failure, and the mode of failure.

Several empirical, analytical, and numerical models have been created recently to better understand and simulate the processes involved in breaching earth-fill dams and their

breach characteristics. In this regard, hydraulic models have been utilized with different sediment transport and erosion formulas (Fread 1988; Visser 1998; Ponce and Tsivoglou 1981; Wang and Bowles 2006; Faeh 2007). These physical breach formation models intended to explain the physical mechanisms behind failures. However, they can be difficult to initiate in cases where a lower degree of complexity is required (Froehlich 2008). As an alternative, Pierce et al. (2010), Walder and O'Connor (1997), and Froehlich (2016) proposed regression equations derived from statistical analysis of dam studies to estimate the peak discharge. MacDonald and Langridge-Monopolis (1984), Froehlich (2008), Von Thun and Gillette (1990), and Xu and Zhang (2009) have examined numerous dam breach case studies with varying properties and developed distinct empirical equations to determine dam breach parameters based on a simple growing trapezoidal breach shape, which is a commonly observed phenomenon following multiple dam breaches. These parametric models establish the ultimate width, depth, and shape of the breach, as well as the duration required for breach development. On the other hand, simplified physical breach models simulate the temporal changes in the geometry of the dam break. Furthermore, the United States Army Corps of Engineers (USACE 1980) and Federal Energy Regulatory Commission (FERC 1988) have published guidelines based on their respective databases, which can aid researchers in defining the limits of breach parameters and permit engineering judgment to be applied in the decision-making phase.

The models utilized for estimating dam breach often employ a simplified approach to a complex hydromechanical phenomenon influenced by multiple factors, including flow conditions, embankment shape, material characteristics, shear strength of materials, and the degree of homogeneity within the embankment. These factors constitute uncertainties that cannot be precisely determined. Moreover, their influence can lead to variations in breach geometries. To address these uncertainties, Froehlich (2008) and Wahl (2004) conducted analyses for key breach parameters from historical dam failures and provided valuable insights into the range of values that can be considered in risk assessments for dam failures. To account for uncertainties in dam breach modeling, sensitivity analysis is commonly used (e.g., Haltas et al. 2016; Basheer et al. 2017). In sensitivity analysis, breach parameters are increased as percentages, and the results are separated into worst-case and best-case scenarios. While sensitivity analyses can be useful to identify potential consequences, in some cases, using such wide ranges to describe dam break parameters may lead to overly conservative results. In this context, Goodell et al. (2018), as a recent approach, suggests that probabilistic dam break modeling can address these concerns by fitting statistical distributions to the input parameters used in dam break simulations. Therefore, in modeling dam-break scenarios, it can be advantageous to construct a probabilistic model that predicts the peak flows having different exceedance probabilities, instead of relying solely on deterministic approaches. For example, Sarchani and Koutroulis (2022) conducted a Monte Carlo simulation by selecting a plausible range of parameters and conducted flood inundation analyses for seven different exceedance probability scenarios. Rizzo et al. (2023) proposed a probabilistic method by assigning different dam breach width and reservoir parameters to hypothetical break of Mignoni Dam, where a weight assigned to each scenario to define conditional probability of a dam-break event.

Furthermore, it is crucial to assess the downstream impacts of a dam collapse to identify high-risk areas and formulate emergency evacuation strategies for the residents. In this regard, hydraulic numerical models of one-dimensional (e.g., Pilotti et al. 2011; Guido et al. 2023), two-dimensional (e.g., Tsakiris and Bellas 2014; Yilmaz et al. 2023), and integrated 1D/2D models (e.g., Pasquier et al. 2019; Jibhakate et al. 2023) are commonly employed in the literature. Although 1D models are faster compared to

2D models, they cannot adequately represent flood wave diffusion on floodplains having complex topographic conditions and might be disadvantageous for the cases which water flow path is ambiguous (Ahmad and Simonovic 1999). Moreover, the outputs of hydraulic model simulation associated with dam breach are used in quantitative flood hazard assessment. According to the EU Flood directive, flood hazard is quantified by an inundation map of the affected area, while in practice researchers, such as Mani et al. (2014), include flood velocity, depth and flood duration as decisive factors. In addition, many countries and government agencies have adopted heuristic or empirical flood hazard classification systems. United States Bureau of Reclamation (USBR) (1988) conducted a study of hazard classifications and derived charts about depth-velocity-flood damage relationships for humans. Smith et al. (2014) made an extensive study including experiments with real objects and derived distinct flood areas divided by curves depending on the association of impacts of the flood on real people, cars, and buildings. Some other methods, including artificial neural networks (e.g., Tien Bui et al. 2016), machine learning techniques (e.g., Antzoulatos et al. 2022) and multi-criteria decision analysis (e.g., Hagos et al. 2022) were also used to classify the level of flood hazards in the field. Moreover, existing literature includes several studies on flood hazards linked to dam breach scenarios similar to the one examined in this study. For instance, Bilali et al. (2022) analyzed the probabilistic flood hazards resulting from dam breaches in a case study in Morocco, employing a combination of hydrologic and hydraulic models. Rizzo et al. (2023) created probabilistic flood inundation and hazard maps using a 2D hydraulic model for a hypothetical dam failure in Italy. Additionally, Bello et al. (2024) integrated hydrologic and hydraulic models for a watershed in Nigeria, identifying hazards related to dam failure based on flow velocities and depths.

The analysis of a dam break involves several steps, such as predicting breach parameters and approach, routing inflow through the reservoir, simulating flood inundation downstream, and conducting flood hazard and risk assessments. This study focuses on the Kanlikoy Dam, an earth-fill dam located in Nicosia, Cyprus. The primary aim of this study is to determine flood inundation and hazard zones in the urbanized area downstream of the Kanlikoy Dam resulting from possible dam breaches, while taking into account various scenarios of piping and overtopping failures. This study stands out as pioneering and comprehensive research in the domain of dams in northern part of Cyprus, primarily for its integration of hydrologic modeling in a data-limited setting and its site-specific risk assessment utilizing a 2D hydraulic model. Undertaking similar studies in data-sparse regions is rare due to challenges such as limited data availability, a lack of reliable information, and other associated issues, which are less common compared to developed countries. In this context, hydrologic models were established to obtain hydrographs of specific rainfall events with a 100-year return period and probable maximum precipitation for use in dam failure scenarios. These hydrographs were subsequently defined as boundary conditions in 2D HEC-RAS models, which simulated the propagation of flood waves to discern the failure mechanism and consequences in Nicosia. Each breach parameter was presumed to adhere to a particular statistical distribution, hence producing multiple exceedance probability scenarios of dam breach hydrographs. The hydrographs were acquired through the utilization of the McBreach software, which executes Monte Carlo simulations encompassing 10,000 iterations. This study has the potential to serve as a reference for stakeholders and decision-makers in comprehending the magnitude of hazards and risk levels associated with dam failure, and to facilitate the development of a risk management plan aimed at mitigating the risks of such an occurrence.

2 Materials

2.1 Characteristics of study area

The selected study area is located in the north-western part of the capital city, Nicosia, the most densely populated city on the island of Cyprus. Cyprus is situated in the Eastern Mediterranean region and has a semi-arid climate, characterized by mild, rainy winters due to westward-moving cyclones and extended periods of hot, dry summers (Hadjinicolaou et al. 2010). The island’s diverse topography, which includes the Kyrenia Mountains running parallel to the north coast, the low-lying Mesaoria Plain in the center, the Troodos Mountains in the south, and the Karpass Peninsula, results in significant local variations in meteorological conditions, such as precipitation patterns (Zaifoglu et al. 2017). The study area of the Kanlikoy Dam catchment extends from the hills of the Kyrenia Mountains in the north towards the Kanlikoy Reservoir, following the Cinardere (Jinar) Creek, which passes through the village of Kanlikoy and the town of Gonyeli in the Nicosia district, as illustrated in Fig. 1.

The downstream area of the catchment has experienced rapid urbanization in recent decades, characterized by the construction of small and medium-sized residential areas. Flash flooding is a significant problem in the study area, attributable to the climatic conditions of the region and the increasing proportion of impervious surfaces, leading to severe flood events in 2010, 2014, and 2021. The research is focused on the Kanlikoy Dam, which is a homogeneous earthen-embankment dam composed of silty clay material and features a gravel and sand filter blanket. Originally built as a small embankment for the purpose of irrigating agricultural fields, it was later replaced due to a reduction in capacity of up to

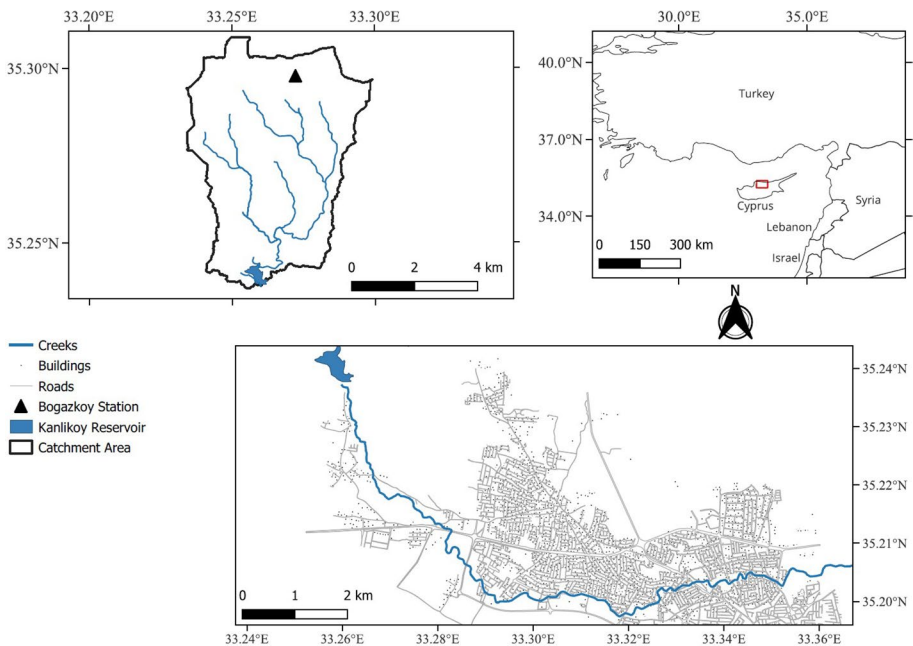


Fig. 1 Study area

30% caused by the silting process. The current embankment stands at a height of 12.36 m from Talweg to crest and has a crest length of 297 m (Konteatis 1974). The dam has a reservoir capacity of approximately 1 million m³ and is equipped with a spillway capable of releasing water at a rate of 110 m³/s. The summary of the characteristics of Kanlikoy Dam is given in Table 1. The reservoir is directly linked to the Cinardere Creek, which is an ephemeral stream and partially obstructed in some areas. The lack of investigation of the embankment material prevents conducting more detailed stability assessments that require parameters related to soil strength, erodibility, and permeability.

2.2 Data acquisition and processing

The dataset utilized in this study has been classified into two distinct categories, namely, the topographic and hydrologic datasets. Initially, the construction of the terrain model was accomplished through the utilization of Digital Elevation Model (DEM) along with the surveyed channel cross-sections of the creek. Subsequently, hydrologic datasets required for rainfall–runoff simulations were provided and processed, which comprised soil maps, a land cover map, and daily rainfall data.

The current study employed a DEM of 2.5 m resolution obtained from the Mapping Office of Northern Cyprus to delineate the catchment of the Kanlikoy Dam and model the floodplains downstream side of the dam. The DEM was subsequently modified using bathymetric surveys of the reservoir and Cinardere Creek, as well as the dimensions of the hydraulic structures located along the creek, which were previously documented by Zaifoglu et al. (2019). This was achieved by converting creek cross sections and reservoir bathymetry into DEM through triangular interpolation using several tools in QGIS (QGIS 2020) and integrating them into the downstream DEM. Furthermore, obstacles, such as buildings and walls, detected in the floodplain were identified using data obtained from the local municipality. Any absent obstructions were then digitized into shapefiles using satellite observations and were elevated to their respective heights to construct the ultimate model.

Table 1 Characteristics of Kanlikoy Dam (Konteatis 1976)

Dam characteristics	Value
Reservoir area	39.0 ha
Reservoir capacity	1.1 × 10 ⁶ m ³
Crest height from ground	12.4 m
Crest length	297.0 m
Top thickness	6.0 m
Base thickness	70.1 m
Upstream slope	1/3
Downstream slope	½
Spillway capacity	110.0 m ³ /s
Spillway size	18.2 × 1.8 m
Spillway length	27.4 m
Freeboard	1.8 m
Outlet diameter	0.3 m
Outlet capacity	0.4 m ³ /s
Outlet length	80.0 m

The hydrologic data employed in this study are the mean daily rainfall, covering the period of 1976–2019, recorded at the Bogazkoy Station situated within the catchment area of the dam. This data was obtained from the Meteorological Office of Northern Cyprus with the aim of creating the design hyetographs in the hydrologic model, based on the Soil Conservation Service (SCS) Type II rainstorm distribution. The present study utilizes the ESA World Cover 2020 (Zanaga et al. 2021), a high-resolution (10 m) raster-based land cover product, derived from Sentinel-1 and 2 data, to identify the downstream coverage. In addition, Curve number (CN) maps of the reservoir catchment area were developed using digitized soil maps generated by local authorities. The CN maps represent the catchment area as predominantly composed of hydrologic soil groups C and D, which are characterized by high percentages of clay content at the surface texture, indicating high run-off potential and low infiltration rates in the Kanlikoy Dam catchment.

To determine the roughness coefficients, which are critical for modeling the flow resistance, the average Manning’s roughness coefficient classification proposed by Papaioannou et al. (2018) was employed as given in Table 2. The classification was based on CORINE (2018) land cover data and matched with the descriptions of land cover areas in ESA World Cover 2020. The Manning’s roughness coefficients of the creek channels were assigned in a raster format, referring to the measurements of Zaifoglu et al. (2019). Additional adjustments and revisions were implemented on the coefficients during the calibration process of the model.

3 Methodology

The phenomenon of dam break events is known to be influenced by multiple parameters and factors, resulting in a complex and uncertain modeling process. Since deterministic models have limited capacity to quantify the associated uncertainty levels, a probabilistic approach that integrates all relevant sources of uncertainty across various contributing factors can provide estimates of exceedance probabilities for the dam breach hydrographs as well as the downstream flood hazards. In this regard, flood modeling associated with different dam break scenarios is carried out according to a flowchart as given in Fig. 2. The following sequence of steps has been executed in a general sense: Firstly, a rainfall frequency analysis was conducted

Table 2 Manning’s roughness coefficients for land covers in study area

Land cover class	Manning roughness coefficient (<i>n</i>)
Tree cover	0.100
Shrubland	0.070
Grassland–Shrubland	0.040
Cropland	0.030
Built-up (residential)	0.060
Sparse vegetation	0.035
Permanent water	0.050
Wetland	0.080
Dam break buffer zone	0.200
Asphalt roads	0.013

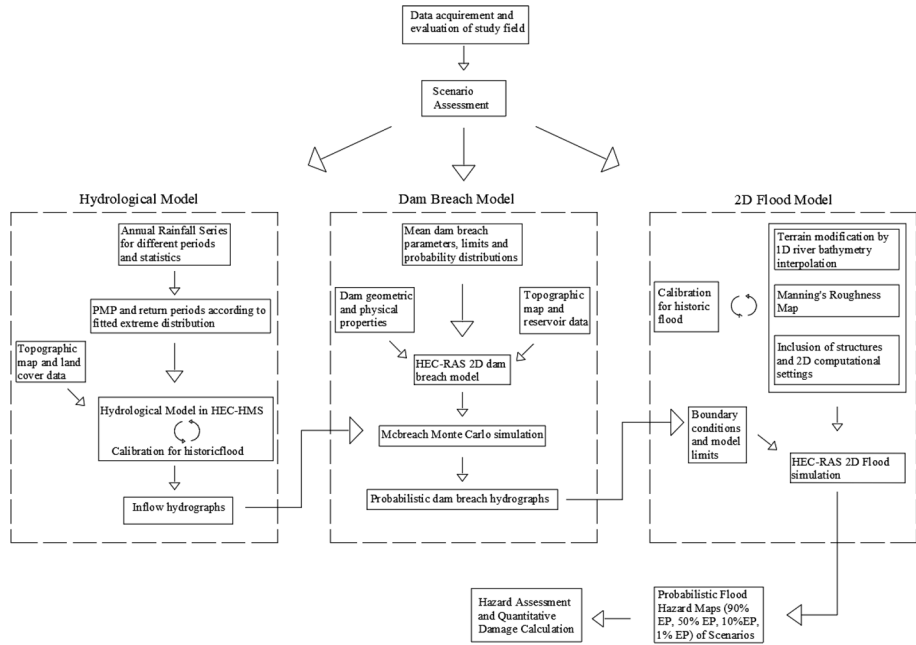


Fig. 2 Flowchart of the adopted methodology

to estimate both the probable maximum precipitation and extreme rainfall events with a 100-year return period. Subsequently, hydrologic modeling was performed to generate inflows based on different scenarios. Next, probability distributions were fitted to the dam breach parameters, which were then sampled using Monte Carlo simulations. Finally, dam breach flood hydrographs were specified as boundary conditions in 2D HEC-RAS models, which were employed to generate several flood hazard maps corresponding to various exceedance probabilities.

3.1 Hydrologic modeling

3.1.1 Rainfall frequency analysis

In this study, statistical frequency analysis was employed to estimate the rainfall quantiles for use in relevant scenarios. Several common probability distributions, such as Generalized Extreme Value (GEV), Extreme Value Type I (Gumbel), and Weibull distributions, were fitted to the annual maximum rainfall series (AMRS) of the representative Bogazkoy station. The goodness of fit of these distributions was evaluated using two hypothesis tests: the Chi-square (χ^2) and Kolmogorov–Smirnov test with a significance level of $\alpha = 0.05$. The GEV Type II distribution was found to be the most successful. The cumulative distribution function of GEV Type II is provided as:

$$F(x; \mu, \sigma, \xi) = \exp \left(- \left[1 + \xi \frac{(x - \mu)}{\sigma} \right]^{-\frac{1}{\xi}} \right) \tag{1}$$

where ξ , μ and σ represent a shape, location, and scale parameters of the distribution function, respectively. The estimated parameters were determined to be $\xi = 0.268$, $\mu = 44.84$ and $\sigma = 21.60$, where the maximum rainfall depth with a 100-year return period equals 241 mm/day. Moreover, the Probable Maximum Precipitation (PMP) was estimated using the Hershfield method (1965) based on the assumption that the return period of a Probable Maximum Flood (PMF) event is equivalent to that of a PMP event (Wright et al. 2020). The Hershfield method is reliable and effective in estimating PMP, particularly when sufficient precipitation records are available. It proves particularly beneficial in rural and data-sparse regions like Northern Cyprus, as it does not depend on additional meteorological variables for PMP calculation. The method is expressed as follows:

$$PMP = X + K_m \sigma' \tag{2}$$

where K_m is frequency factor specific to site, and X and σ' are average and standard deviation of annual maximum rainfall series, respectively. In accordance with the recommendation of the World Meteorological Organization (WMO 2009), an enveloping technique was used to estimate PMP, and K_m was modified by drawing a specific regional enveloping curve, as demonstrated in Fig. 3, for the region under investigation (e.g., Rakhecha et al. 1992; Boucefiane and Meddi 2022). The maximum daily rainfall series obtained from 36 meteorological stations located in Northern Cyprus analyzed to find the value of K_m , which was determined to be 8.15. Furthermore, PMP was estimated to be 480 mm, corresponding to a 1020-year return period.

3.1.2 Rainfall–runoff modeling

The HEC-HMS software, which can execute comprehensive hydrologic analysis integrated with geographic information system (GIS) techniques, was employed for the purpose of rainfall–runoff simulation modeling. Within the HEC-HMS framework, essential processes, such as sink and drainage processing, as well as the identification and delineation of streams, were proficiently executed. Specifically, a detailed basin model comprising eight sub-basins, each covering an area ranging between 1 km² and 6 km², interconnected by drainage streams was acquired. The total catchment area of Kanlikoy Dam was estimated to be approximately 34.1 km².

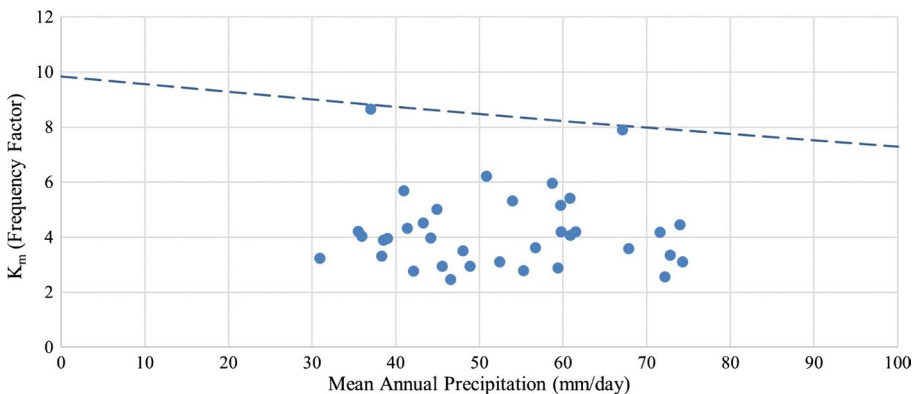


Fig. 3 Frequency factor curve of region

The hydrologic modeling process comprises three primary steps: computation of rain-fall losses through the SCS CN method, flood routing in streams using the Muskingum method, and transformation of runoff through the SCS Unit Hydrograph (UH) technique (SCS 1972). The subbasin curve numbers were assigned through histogram analysis conducted on digitized maps. The primary coefficients of the Muskingum method were initially selected as typical average values, and they were subsequently adjusted in the calibration phase based on a reference flood event of 2010 Flood. Considering the available datasets, applicability, and convenience, the SCS UH method was chosen for the runoff transformation. Herein, the physical catchment properties required were obtained using GIS applications in HEC-HMS. Moreover, the daily rainfall data was utilized and distributed in accordance with the SCS Type II synthetic rainfall distribution. After analyzing 66 hourly measurements of various storm events in the basin from 2010 to 2015, the storm duration was established at 12 h, indicating an average duration of heavy precipitation events to be approximately 12 h based on historical data.

Once the model was constructed, the rainfall–runoff relationship was calibrated in accordance with the hydrograph for the 2010 Flood that occurred after consecutive wet days. The objective of the calibration was to match time to peak and magnitude of peak discharge with the 2010 Flood event, in scope of representing the conditions of the event day. The initial Muskingum coefficients of identified streams were optimized by minimizing the peak-weighted root mean square error (RMSE) function. The model's performance was then evaluated using the Nash–Sutcliffe efficiency (NSE) and the percent deviation in peak discharge ($\% \Delta Q_p$) as follows:

$$NSE = 1 - \frac{\sum_{t=1}^T (Q_o^t - Q_m^t)^2}{\sum_{t=1}^T (Q_o^t - \bar{O})^2} \quad (3)$$

$$\% \Delta Q_p = \frac{|Q_p^s - Q_p|}{Q_p} \times 100 \quad (4)$$

where Q_o and Q_m are the observed and modeled stream flows at time step t , respectively, \bar{O} is the mean observed stream flow over the simulation period, Q_p is observed peak discharge and Q_p^s is simulated peak discharge.

3.2 Hydraulic modeling

3.2.1 Dam breach modeling

The parameters associated with dam breach constitute a vital component of dam failure analysis. These parameters encompass various attributes pertaining to the occurrence of dam failure, including the size and shape of the breach, the failure mode, breach weir coefficient, and the time of breach formation. The probabilistic modeling of dam breach was evaluated using the McBreach software, which employs Monte Carlo simulation to randomly sample breach parameters in accordance with predefined statistical distributions. Peak discharges are then extracted based on their corresponding exceedance probabilities within the sampled breach dataset, as outlined by Goodell (2019).

In order to establish a reference for the parameter random samples, the parameters determined by Froehlich’s empirical method (2008) are selected as given in Table 3. This decision was made on the basis that the example case database utilized in this method aligns closely with the properties of the Kanlikoy Dam embankment. Rather than employing specific parameters, a range of values for each ambiguous parameter was selected and distributed randomly. The assessment of the distribution of breach parameters and their ranges were primarily dependent on engineering judgement with consideration of certain physical limitations, and a combination of parameter guidelines in FEMA (2013), the HEC-RAS Manual (Brunner 2014), standard errors of parameters within Froehlich’s (2008) method, and site conditions of the embankment as shown in Tables 4 and 5, for overtopping and piping failure respectively. The single deterministic parameter in each scenario is the final bottom elevation, consistently set to match the elevation of the immediate tailwater grid of the embankment dam. Also, for different scenarios, McBreach was run 10,000 times by defining the respective breach parameters and inflow hydrographs, and at the end, dam

Table 3 Breach parameters according to Froehlich (2008)

Parameters	Piping	Overtopping
Breach bottom width (m)	18	28
Side slopes (H:V)	0.7	1.0
Formation time (h)	0.63	0.87

Table 4 Breach parameters of overtopping failure

Parameters	Sampling type	Distribution	Mean	Lower limit	Upper limit	Standard deviation
Final bottom elevation (m)	Deterministic	–	167.8	–	–	–
Breach width (m)	Probabilistic	Normal	28	12	60	8
Side slopes	Probabilistic	Normal	1	0.7	1.3	0.1
Formation time (h)	Probabilistic	Normal	0.87	0.35	1.2	0.15
Breach weir coefficient	Probabilistic	Uniform	–	1.1	1.8	–
Breach initiation elevation (m)	Probabilistic	Uniform	–	175.4	176	–

Table 5 Breach parameters of piping failure

Parameters	Sampling type	Distribution	Mean	Lower limit	Upper limit	Standard deviation
Final bottom elevation (m)	Deterministic	–	167.8	–	–	–
Breach width (m)	Probabilistic	Triangular	18	12	60	–
Side slopes	Probabilistic	Normal	0.7	0.4	1	0.1
Formation time (h)	Probabilistic	Normal	0.63	0.2	1	0.15
Breach weir coefficient	Probabilistic	Uniform	–	1.1	1.8	–
Breach initiation elevation (m)	Deterministic	–	173.9	–	–	–
Piping coefficient	Probabilistic	Uniform	–	–	0.6	–
Initial piping elevation (m)	Probabilistic	Uniform	–	167.8	173.9	–

breach flood hydrographs of pre-defined exceedance probabilities of 90%, 50%, 10%, and 1% were derived. It is noteworthy to state that a total of 10,000 Monte Carlo trials proved sufficient to satisfy the convergence criteria of differential statistics.

3.2.2 Flood modeling

The present study employed the 2D HEC-RAS (version 6.3) to perform unsteady flow computation. The model was designed to utilize breach hydrographs as input boundary conditions, with the aim of observing the downstream consequences of the breach flood wave. The 2D shallow water equations (SWE) were selected for this purpose, as it employs 2D full momentum equations. This computation methodology is better suited than the dynamic wave routing method for rapidly increasing dam break waves due to its inclusion of essential local and convective acceleration terms (Brunner 2020). The computational mesh structure was developed to satisfy model stability, which cumulatively equivalent to approximately 300,000 mesh with varying dimensions from 2.5 m × 2.5 m in the streams to 15 m × 15 m on specific parts of floodplain which were relatively far from the channel. The Courant number (C), which is suggested in dam break studies can be expressed as follows (Brunner 2014):

$$C = \frac{V_w * \Delta T}{\Delta X} \leq 1 \quad (5)$$

where V_w is flood travel velocity, ΔT is time step, and ΔX is distance between mesh structures. In the simulation, time step automation was employed, with an initial time step of 2 s, to ensure that the Courant number remained between 0.45 and 1. Therefore, the time step value was automatically adjusted to maintain the specified range.

3.2.3 Flood hazard assessment

When evaluating flood hazard, factors, such as inundation, depth, and velocity are critical indicators in assessing severity and impact. Safety concerns for individuals, properties, and structural inventory become a significant priority during floods, particularly during huge floods with enormous peak values. This study employed a hazard classification system based on the product of the maximum depth and velocity within the inundation boundaries of each probabilistic scenario. To classify separate regions based on their hazard level, the study conducted by Smith et al. (2014) was utilized. The hazard classification, description, and classification limit values are given in Table 6. Additionally, flow depth and velocity maps were generated within the inundation boundaries for each exceedance probability to quantify the risks in detail.

3.3 Scenarios for analysis

Three distinct dam break scenarios were developed considering realistic worst-case situations that can be classified into two categories: sunny day failure due to piping, and rainy-day failure caused by extremely catastrophic events, such as a 100-year rainfall and probable maximum precipitation resulting in overtopping. In this study, the possibility of the piping scenario was initially assessed by varying the hydraulic conductivity parameters of the embankment silty-clay material in a steady state finite element analysis using the Slide2 software. The analysis revealed maximum exit hydraulic gradient values of up to

Table 6 The flood hazard classifications, descriptions, and classification thresholds adopted from Smith et al. (2014)

Flood hazard classification	Description	Classification thresholds
H1	Generally safe for vehicles, people and building	$D \times V \leq 0.3$
H2	Unsafe for small vehicles	$D \times V \leq 0.6$
H3	Unsafe for vehicles, children and the elderly	$D \times V \leq 0.6$
H4	Unsafe for vehicles and people	$D \times V \leq 1.0$
H5	Unsafe for vehicles and people. All buildings vulnerable to structural damage	$D \times V \leq 4.0$
H6	Unsafe for vehicles and people. All building vulnerable to failure	$D \times V > 4.0$

2.7, indicating the presence of a significant risk of piping failure under full-reservoir conditions. The details of each scenario are as follows:

Scenario 1. Sunny Day/Piping Failure Scenario: This scenario is specifically designed to simulate a piping failure caused by a hydraulic gradient issue, with the water level in the reservoir assumed to be full at spillway crest elevation. Notably, rainfall is not considered as a factor in this scenario. Furthermore, the absence of other flood-related processes that could have already caused damage or issued evacuation warnings emphasizes the importance of taking this scenario into account.

Scenario 2. 100-year rainfall/Overtopping Failure: This scenario focuses on the rainy-day failure, which takes into account the situation when a reservoir is full and experiences an extreme inflow. This inflow is caused by a rainfall event that has a return period of 100 years and may activate the overtopping failure mode. Additionally, there is often a greater amount of forewarning and time for evacuation in rainy days, which further mitigates potential damage.

Scenario 3: Probable Maximum Precipitation/Overtopping Failure: The present scenario involves assuming the occurrence of a Probable Maximum Precipitation event, which has the potential to trigger a maximum possible flood. Given the volume of rainfall and the capacity of the reservoir, it is highly probable that such an event would result in overtopping failure, with any reservoir water level considering its capacity.

4 Results and discussion

4.1 Hydrologic modeling results

In order to generate inflow hydrographs for dam breach scenarios, meteorological inputs of 100-year return period and Probable Maximum Precipitation in terms of daily rainfall were defined as input into hydrologic model. These cumulative rainfalls were then distributed in accordance with SCS Type II rainfall distribution over a 12-h storm period. The detailed basin model is shown in Fig. 4, which was developed and calibrated using the procedures outlined in Sect. 3. In this regard, firstly, a DEM was processed to obtain a hydrologically accurate terrain for the delineation process. Subsequently, flow direction raster, indicating the flow direction between grid cells, and flow accumulation raster, showing the

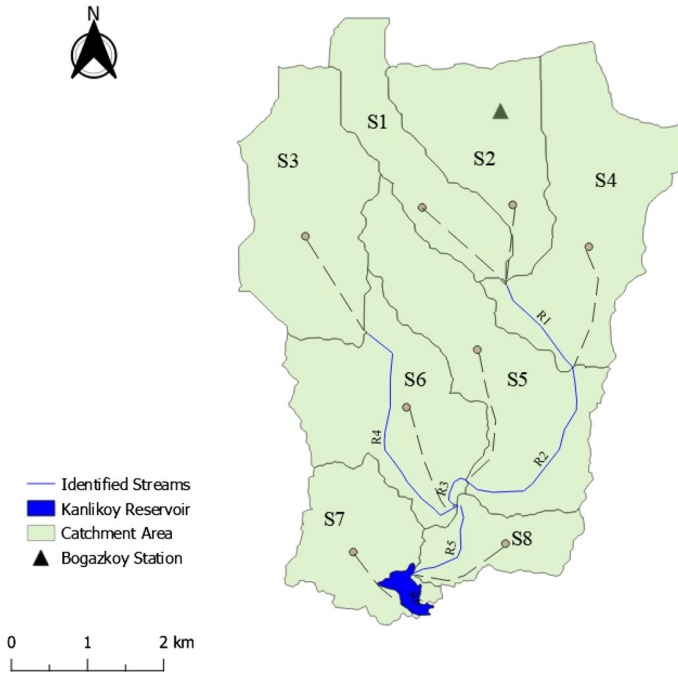


Fig. 4 The sub-basins of Kanlikoy Dam catchment in hydrologic model

accumulation of upstream cells, were derived from the DEM to identify streams. Streams were then obtained based on a threshold of 1 km^2 drainage areas. This step, combined with the specification of outlet points, facilitated the creation of a sub-basin and reach network. Ultimately, eight sub-basins were delineated, forming a basin model that accurately represents the detailed interactions influenced by topography and geographical barriers.

Table 7 presents a detailed overview of the spatially calculated properties of the sub-basins within the Kanlikoy Dam catchment. The lag time and time of concentration required for the SCS UH transformation method were determined based on the

Table 7 The characteristics of basin models

Basin	Curve number, CN	Longest path length (km)	Average basin slope (%)	Time of concentration, t_c (h)	Basin area (km^2)
S1	80.0	5.10	21.0	2.63	3.52
S2	78.1	4.04	28.6	1.90	2.80
S3	81.5	4.78	19.1	2.59	5.55
S4	74.0	5.12	16.9	3.11	5.47
S5	89.7	5.49	7.9	4.21	4.93
S6	89.2	4.34	8.6	3.36	4.66
S7	89.1	3.26	14.8	2.04	1.68
S8	88.5	3.06	14.6	1.96	2.81
Kanlikoy Dam	83.3	13.45	15.8	6.42	31.41

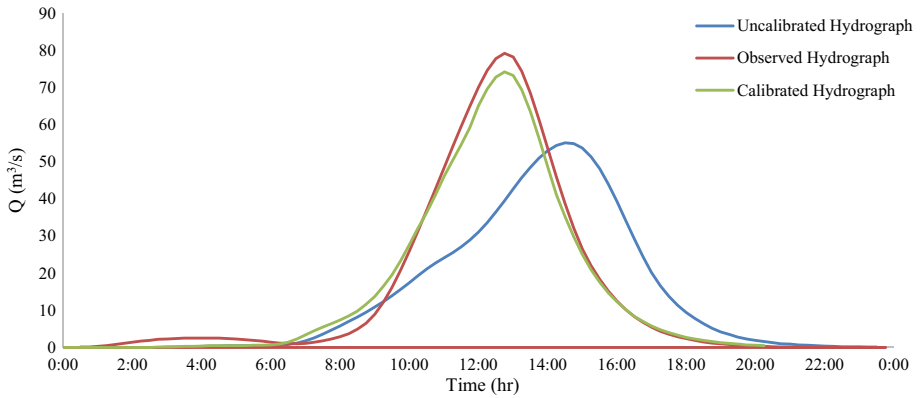


Fig. 5 Calibrated runoff model performance compared to 2010 flood hydrograph

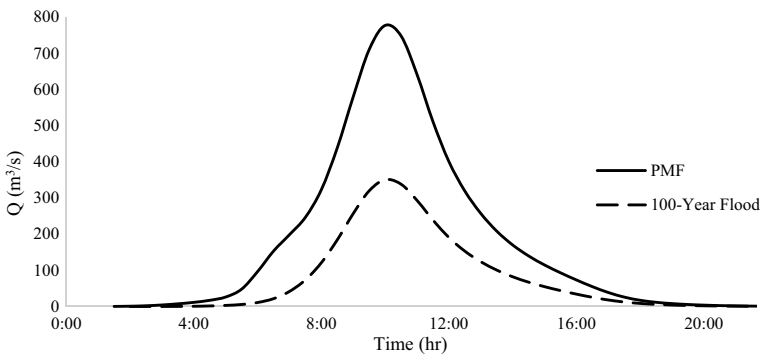
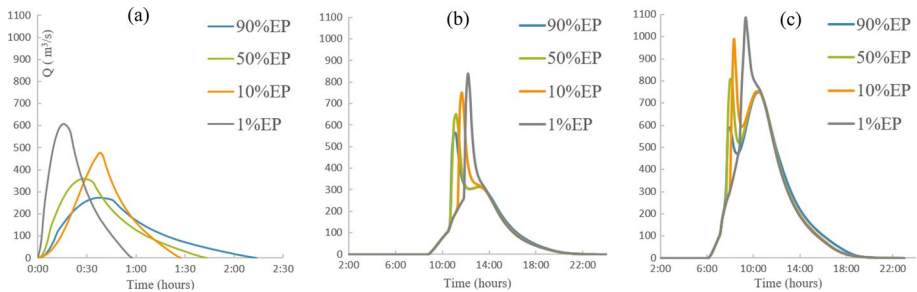


Fig. 6 The estimated runoff hydrographs

methodology outlined by the SCS (1972). The basin model was established by selecting an outlet point on the dam site, and flood routing parameters of identified streams, Muskingum parameters, were calibrated using the 2010 Flood event as a reference. After a number of trials, the parameters of K and x , influencing flood routing for each sub-basin, and lag time of sub-basin S7, the sub-basin directly linked to reservoir, were optimized up to a satisfactory level. Based on the performance assessment criteria, the percent deviation in peak discharge ($\% \Delta Q_p$) of raw model was reduced from 30.43% to 6.31%, and NSE of raw model was increased from 0.598 to 0.969, after the calibration. The hydrographs of the reference flood event, uncalibrated, and calibrated models are demonstrated in Fig. 5. Moreover, it was assumed that the ground surface of the catchment area would be wet with reduced abstraction capacity during hydrologic simulations, replicating the conditions of 2010 Flood event. Herein, the results suggested that the resulting Probable Maximum Flood scenario produced a peak discharge of $776 \text{ m}^3/\text{s}$ and a cumulative runoff volume of $13.48 \times 10^6 \text{ m}^3$, while the 100-Year Flood scenario yielded a peak discharge of $351 \text{ m}^3/\text{s}$ and a total runoff volume of $6.1 \times 10^6 \text{ m}^3$. The resultant hydrographs obtained for these scenarios, presented in Fig. 6, were then utilized in the dam breach simulations.

Table 8 The peak discharges for each scenario and exceedance probability

Scenario	Exceedance probability peak discharges (m ³ /s)			
	1% EP	10% EP	50% EP	90% EP
1	607.36	475.94	359.65	273.47
2	839.44	749.74	651.41	561.84
3	1082.8	985.63	805.36	749.13

**Fig. 7** Dam breach hydrographs of **a** Scenario 1, **b** Scenario 2, and **c** Scenario 3, respectively

4.2 Dam breach scenarios

Using the same geometry generated in HEC-RAS, different dam breach models including several combinations of dam breach parameters for each scenario were employed in McBreach software. For each scenario, the breach initiated from the middle of the embankment, where the lowest tail elevation was observed. To ensure the verifiability of the reservoir routing, mass conservation was checked for each scenario, and the total error in neither case exceeded 0.5%. Therefore, it was ensured that all hydrographs under the same scenario were identical in terms of volume.

Table 8 shows the peak discharges associated with various exceedance probabilities for three distinct scenarios. The peak discharge for each exceedance probability differed significantly from one another, with Scenario 1 exhibiting the widest range of peak discharge between 273.5 m³/s and 607.4 m³/s. In both Scenarios 2 and 3, each EP hydrograph exhibited an identical curve until the breach formation, as the same spillway coefficient was utilized for all EP cases, resulting in the generation of identical overtopping discharges. In Scenario 1, the hydrograph of the 1% EP case with the highest discharge had the smallest time to peak, dependent on the time of formation. However, time to peak does not demonstrate a general trend, as shown in Fig. 7, where other geometric properties of the breach also influence the peak discharge values since EP cases do not follow the time to arrival order. For example, Bellos et al. (2020) emphasized that formation time of breach is a critical parameter that considerably influences the characteristics of the maximum breach hydrograph.

Hydrographs of wet day scenarios (Scenario 2 and 3) had a descending order of time to peak with peak discharge increasing as time to peak increases. This was directly related to the contribution of inflow to the breach discharge. The inflow volume was substantially greater than the reservoir capacity, leading to the time it takes to withstand the volume of water overtopping the embankment becoming the governing factor instead of the geometric

properties of the breach shape. Additionally, regardless of the EP cases, Scenario 3 had the highest peak discharges, followed by Scenario 2 and Scenario 1. Furthermore, the 90% EP and 50% EP hydrographs in Scenario 3 demonstrated two peak values, owing to the inflow peak discharge exceeding the original breach discharge.

4.3 Comparing flood inundation results across three scenarios

The flood model was calibrated by referencing the inundation caused by the 2010 Flood event. The 2010 Flood hydrograph was used as an upstream boundary condition for the flood model, along with the surface conditions of the creek and floodplains during that time. While surface roughness characteristics were the primary calibration parameter, adjustments were also made to the terrain at specific small segments of the river and floodplain geometry translations to improve the agreement in these areas. To prevent any potential backwater effects caused by other tributary (Oksuzdere Creek), the calibration area was confined to a specific boundary. The model's goodness-of-fitness, as assessed by calculating the percentage of overlapping flood area, significantly improved from 71.0% to 88.4% after calibration. Besides, as the calibrated flood model reflected the conditions of 2010, it was necessary to modify the model to accurately represent the current terrain conditions for the final model to be used in dam break analysis. Hence, the Manning's roughness coefficients were updated to account for land cover changes and new buildings that have been constructed on the floodplains were added to the terrain. These modifications ensured that the model adequately reflected the current terrain conditions and can be utilized to develop flood inundation maps associated with dam break scenarios.

Flood inundation maps presenting the maximum depth and velocity were generated in raster format following post-processing of exceedance probabilities at 1%, 10%, 50%, and 90% for each scenario. The software QGIS was utilized in the processing steps for raster calculations and map creation. Specifically, Fig. 8 illustrates the downstream flood prone regions, which have been divided into five parts for detailed interpretation. Furthermore, Figs. 9, 10, and 11 present the simulated maximum water depths and inundated area boundaries for Scenarios 1, 2, and 3, respectively. Additionally, Figs. 12, 13, and 14 provide maps of the simulated maximum velocities recorded at each raster cell for the aforementioned scenarios.

The results suggested that Scenario 3 resulted in the largest inundation area, ranging between 3.97 km² and 4.48 km². Meanwhile, Scenario 1 and Scenario 2 had inundation areas ranging from 1.77 km² to 2.23 km² and from 3.02 km² to 3.73 km², respectively. The presence of physical obstructions in the terrain made it challenging to discern differences visually through the maps for inundated areas having different exceedance probabilities. The flood prone regions were identified as single-floor houses in Kanlikoy (Region 1), agricultural area located near the Nicosia-Morphou highway (Region 2), residential area located at the crossroad of LF-53 road (Region 3), and the town of Gonyeli (Regions 4 and 5), as seen in Fig. 8. With the exception of Region 1, all areas showed significant differences of more than 30% as the scenarios changed. Table 9 presents the mean values of maximum depths of the inundated regions, excluding water depths in creek, according to the 1% and 90% EP cases to provide a probabilistic maximum depth range for all scenarios. Upon comparing the 1% and 90% EP cases, variations in mean maximum depths were observed. In Scenario 1, differences ranged from 4 to 30 cm, in Scenario 2 from 12 to 26 cm, and in Scenario 3 from 21 to 25 cm. These findings demonstrated that the greatest variation in maximum depth was detected in Scenario 1. Besides, the maximum water

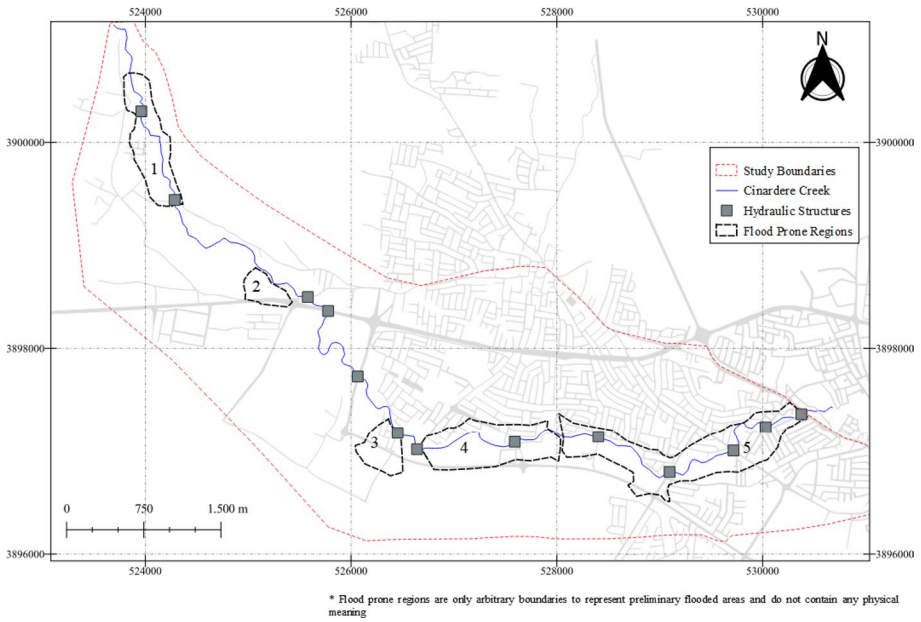


Fig. 8 Flood prone regions

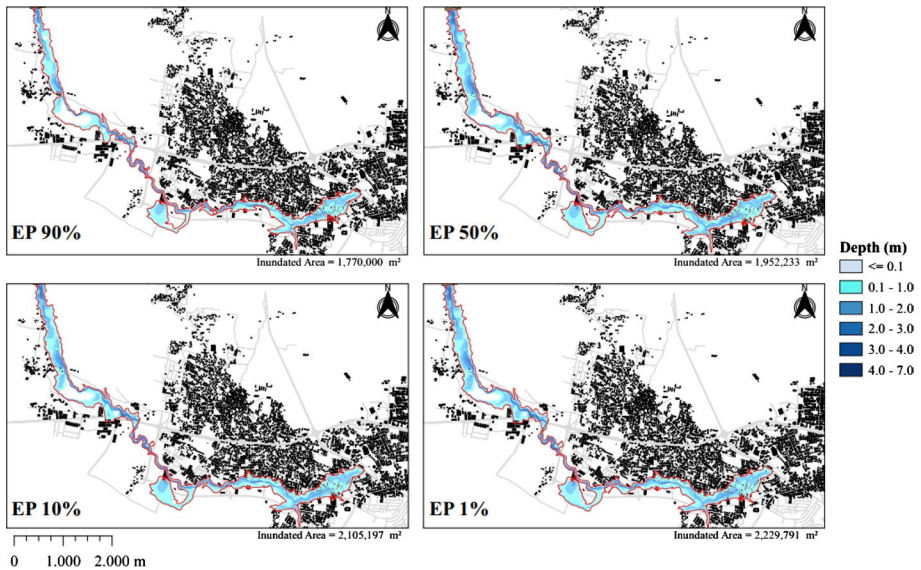


Fig. 9 Maximum depth of Scenario 1

depth recorded was approximately 6.9 m in the dam break buffer zone. In both Scenarios 2 and 3, water depths exceeding 3 m were observed in certain residential areas located in the town of Gonyeli, within a distance of approximately 30 m to 120 m from the creek.

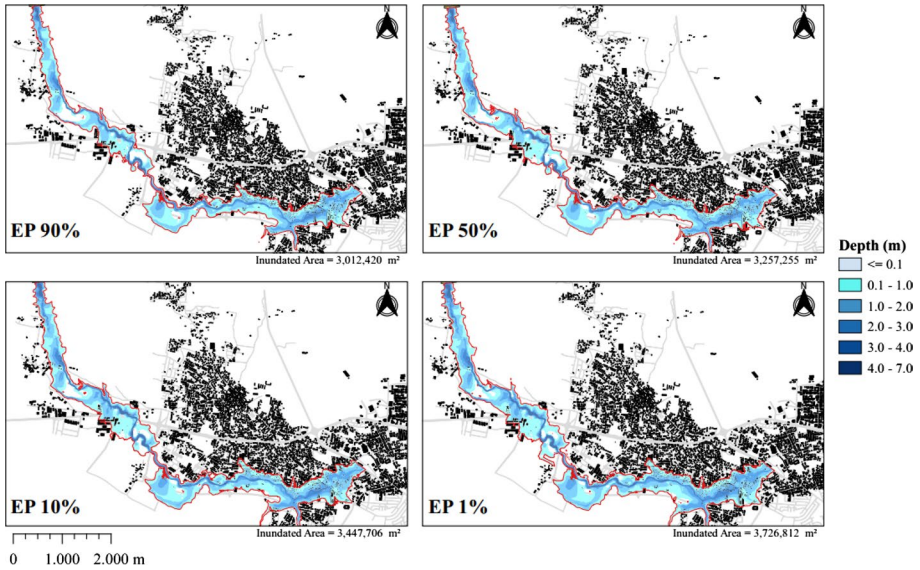


Fig. 10 Maximum depth map of Scenario 2

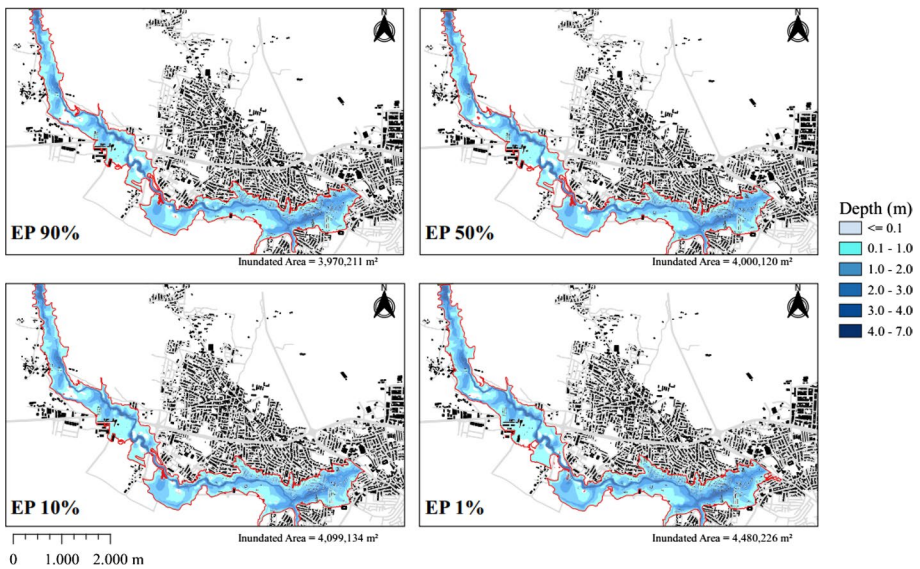


Fig. 11 Maximum depth map of Scenario 3

Additionally, the calculation of inundated areas was performed for specific land use categories including urban and agricultural areas, considering both the 1% and 90% EP cases across all scenarios (Table 10). This analysis provides valuable insights into the affected areas in terms of land cover. It was observed that agricultural areas constituted the majority of the inundated land across all scenarios. However, a notable trend was observed from

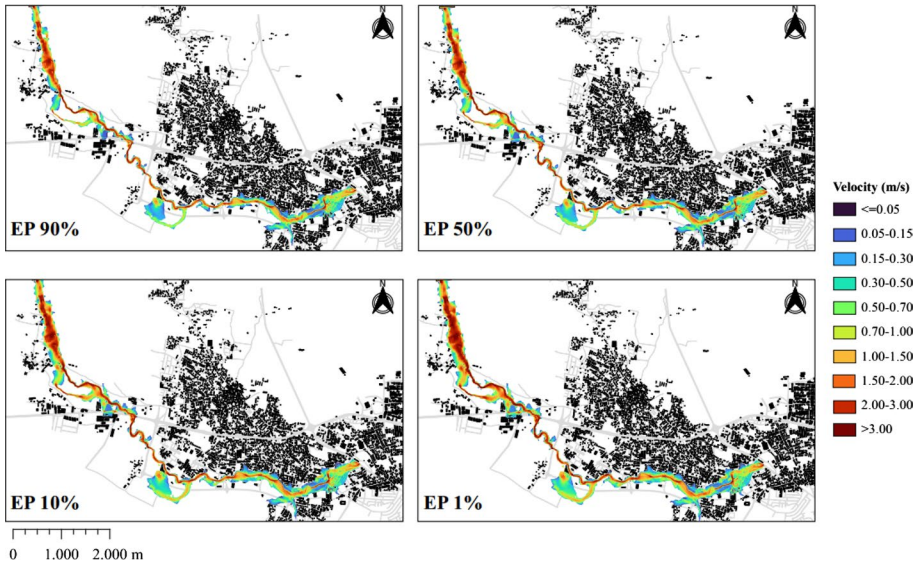


Fig. 12 Maximum velocity map of Scenario 1

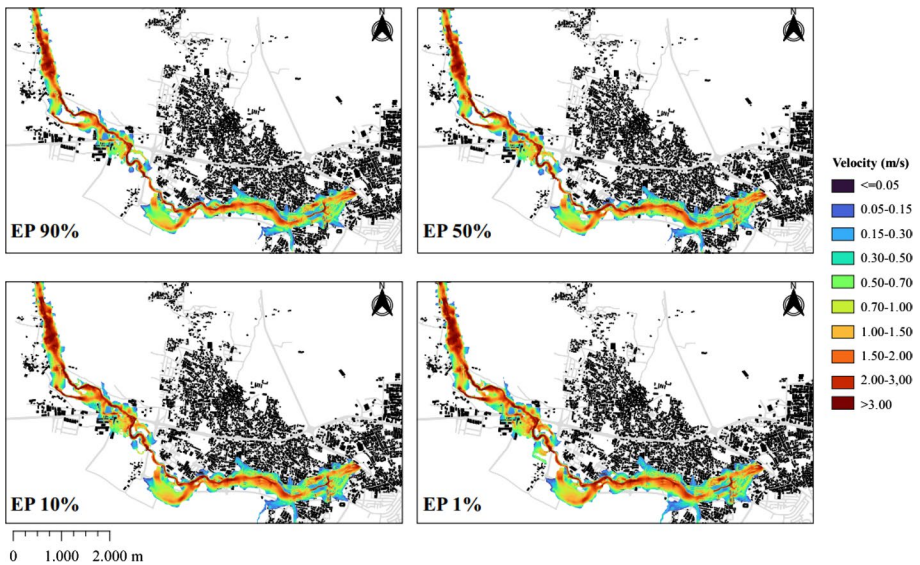


Fig. 13 Maximum velocity map of Scenario 2

Scenario 1 to Scenario 3, where the ratio of agricultural area to residential area decreased. Furthermore, in all scenarios, the ratio of agricultural area to residential area for the 90% EP case was larger than that for the 1% EP case. This suggested that as the inundated area increases, the flood wave propagation tends to affect residential areas more rapidly compared to agricultural areas.

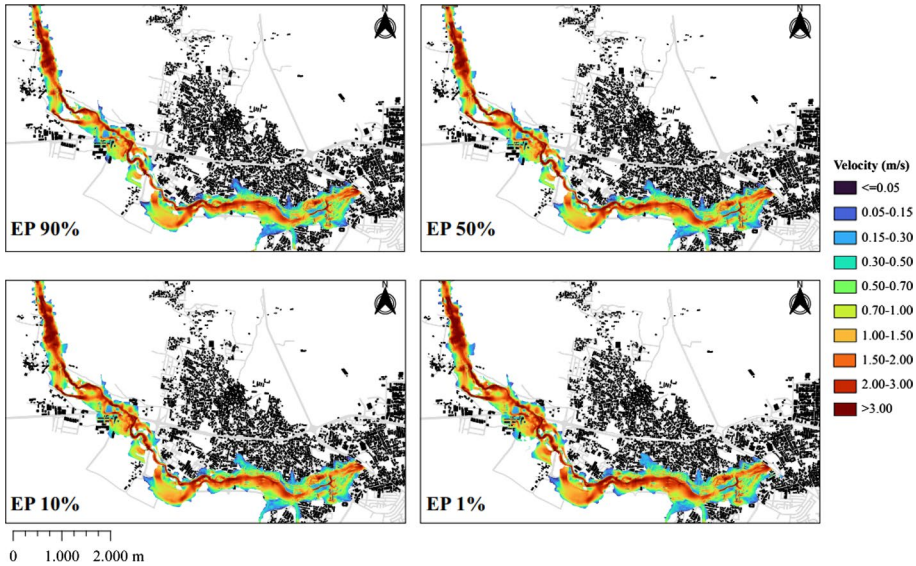


Fig. 14 Maximum velocity map of Scenario 3

Table 9 Mean maximum depths for inundated regions

Inundated regions	Scenario 1		Scenario 2		Scenario 3	
	90% EP	1% EP	90% EP	1% EP	90% EP	1% EP
Region 1	1.02 m	1.32 m	1.36 m	1.62 m	1.56 m	1.87 m
Region 2	0.53 m	0.82 m	1.23 m	1.44 m	1.46 m	1.80 m
Region 3	0.77 m	0.88 m	1.30 m	1.51 m	1.60 m	1.85 m
Region 4	1.21 m	1.25 m	1.37 m	1.49 m	1.59 m	1.78 m
Region 5	0.95 m	1.00 m	1.61 m	1.85 m	2.17 m	2.39 m

Table 10 The inundated agricultural and urban areas for each scenario and specific exceedance probabilities

Regions	Scenario 1		Scenario 2		Scenario 3	
	90% EP	1% EP	90% EP	1% EP	90% EP	1% EP
Agricultural area	699,868 m ²	978,862 m ²	1,297,669 m ²	1,593,500 m ²	1,646,993 m ²	1,896,488 m ²
Urban area	299,775 m ²	387,581 m ²	675,488 m ²	797,112 m ²	901,681 m ²	1,018,643 m ²

Regarding the spatial distribution of maximum velocities, notable variations were observed both among scenarios and within scenarios for different exceedance probability cases. Generally, areas with lower Manning’s roughness coefficients exhibited higher maximum velocity values. However, velocities up to 8 m/s were recorded at the entrance points of culverts and bridges in all scenarios. This suggested that these localized features led to high flow velocities despite energy dissipation. For the rest of the study area throughout

the flood extent, there was a general trend of decreasing maximum velocities, with exceptions observed at areas of constriction, such as between buildings along the flood wave direction or between small-scale local hills and sub-tributaries. While there was a difference of approximately 15% in the EP cases between Scenario 2 and Scenario 3, Scenario 1 exhibited a significant decrease of almost 70% in maximum velocities, particularly in the inundated regions of 1 and 2. This disparity could be attributed to the amount of released water, which plays a significant role in the progression of flow velocities. Unlike the other scenarios, Scenario 1 did not experience a continuous, long-duration flood event.

4.4 Flood hazard analysis

The assessment of flood hazard impact for the scenarios involved the analysis and post-processing of time-dependent depth and velocity maps in raster format. Spatial analyses and raster calculations were conducted using QGIS, and flood hazard maps (Figs. 15, 16, and 17) depicting hazard levels resulting from the failure of Kanlikoy Dam were generated for the scenarios. The impact of the scenarios on the utility system and structure inventory was evaluated by applying a regional hazard classification based on the methodology proposed by Smith et al. (2014), where the definitions within the classification classes were used to identify vulnerability. In this analysis, buildings were considered to be affected regardless of their geometry, size, and purpose of use. For the calculations, structures that received water from at least two sides were assumed as flooded. The percentages of flood hazard levels, total length of inundated roads, which would be rendered unusable during the evacuation process, and the number of buildings at risk of structural damage or failure as a result of the scenarios are presented in Tables 11, 12, and 13, respectively.

Table 12 presents the flood hazard levels for each scenario and exceedance probability. The findings suggested that a potential failure of the Kanlikoy Dam would expose

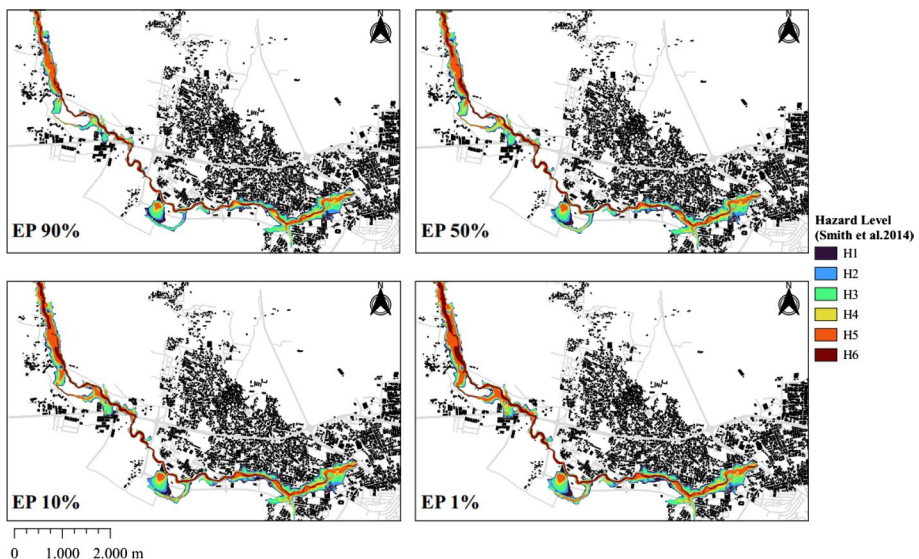


Fig. 15 Hazard classification of Scenario 1

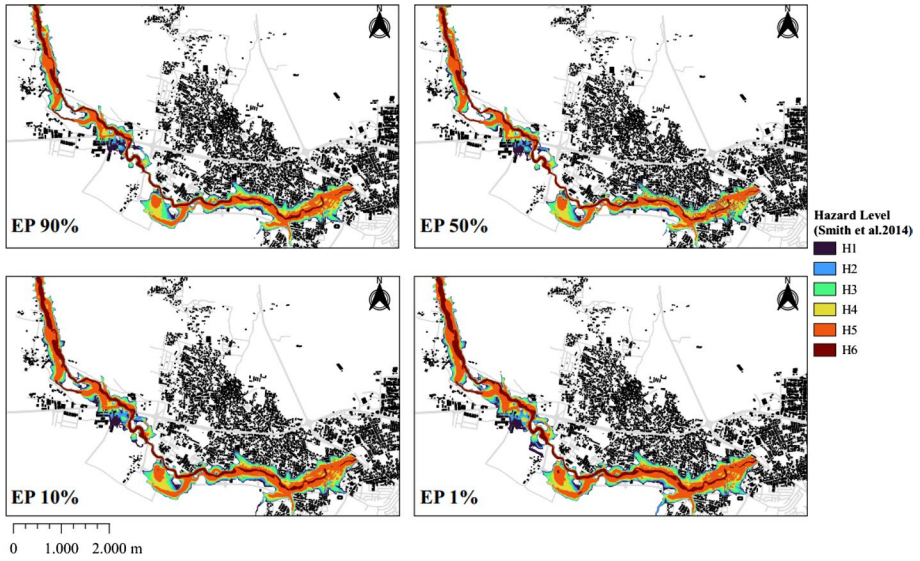


Fig. 16 Hazard classification of Scenario 2

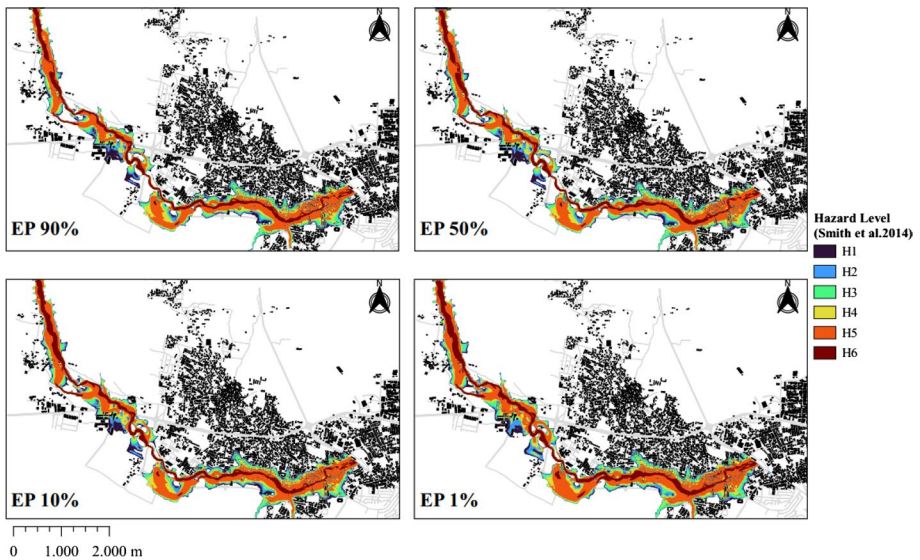


Fig. 17 Hazard classification of Scenario 3

extensive urban areas to significant to high levels of flood hazards. The H5 flood hazard level, indicating the likelihood of structural damage to buildings, was the highest for all scenarios, with a tendency to increase as the exceedance probabilities decreased. In Scenario 1, the H3 hazard level, indicating unsafe flood conditions for vehicles, children, and elderly people, had the second-highest percentage of the inundated area. As

Table 11 The quantitative flood damage for each scenario and exceedance probability

Scenario	Number of flooded structure				Length of inundated roads (m)			
	90% EP	50% EP	10% EP	1% EP	90% EP	50% EP	10% EP	1% EP
1	235	292	326	347	10,483	11,273	12,039	12,343
2	554	636	666	726	19,723	21,117	21,635	23,569
3	842	848	853	935	26,046	26,842	27,425	33,814

Table 12 Percentage areas of hazard types in the inundated areas for each scenario and exceedance probability

Scenario	Hazard classification	Exceedance probability			
		90%	50%	10%	1%
1	H1	15.9	15.1	14.2	13.2
	H2	13.9	13.2	12.7	12.2
	H3	22.6	21.9	20.7	19.2
	H4	13.8	14.4	14.7	14.2
	H5	23.3	23.5	24.8	26.5
	H6	10.6	11.9	12.9	14.8
2	H1	11.5	11.5	11.4	11.4
	H2	9.4	9.5	9.4	9.4
	H3	15.6	15.1	14.3	13.3
	H4	16.9	16.5	15.6	14.8
	H5	33.6	34.2	35.5	36.5
	H6	12.9	13.3	13.8	14.6
3	H1	11.1	11.1	10.5	8.7
	H2	9.1	9.1	8.9	9.1
	H3	13.2	12.9	12.3	12.2
	H4	13.8	13.4	13.1	12.6
	H5	38.1	38.0	38.5	39.2
	H6	14.7	15.6	16.6	18.2

Table 13 The vulnerable structures for each scenario and exceedance probability

Scenario	Hazard level	90% EP	50% EP	10% EP	1% EP
1	H5	10	15	21	24
	H6	0	0	0	2
2	H5	109	111	140	180
	H6	3	3	4	4
3	H5	242	253	258	309
	H6	6	7	7	12

the scenarios progressed towards more severe cases, the hazard levels tended to become more critical. Scenarios 2 and 3 showed the dominant hazard level of H5 followed by H4 and H6, respectively, indicating increasingly hazardous flood conditions for buildings,

people, and vehicles. Consequently, the findings clearly showed that appropriate mitigation measures are necessary to reduce potential flood hazards in these areas.

All hydraulic structures, including bridges and culverts situated along the Cinardere Creek, experienced substantial inflow at their entrances and were found to be susceptible to failure. The maximum hazard level, H6, was observed only within the creek and within a buffer zone of approximately 30 m in all scenarios, indicating that structures located near creeks are more likely to receive a higher hydrodynamic load. As given in Table 11, Scenario 3 exhibited the highest number of flooded buildings and the longest length of inundated roads among all scenarios, ranging between 842–935 buildings and 26.04 km–33.81 km of road length, respectively. Moreover, Table 13 reveals that there were significant variations in the hazard impact on structural inventory among the different scenarios and EP cases. The number of flooded structures increased gradually with the change in scenarios, but the number of vulnerable structures had even more significant differences. Scenario 3 was found to be the most destructive scenario for the structural inventory, with 242, 253, 258, and 309 structures in high hazard levels (i.e. H5 and H6) for the EP cases of 90%, 50%, 10%, and 1%, respectively. However, only two structures in the H6 region were observed in Scenario 1, which only occurred for 1% EP.

4.5 Discussion

Probabilistic modeling is a reliable method to simulate dam-break events and obtain a range of results that reflect the indeterministic and random nature of the failure event. Compared to sensitivity analysis, using a probabilistic framework that includes joint distribution of input parameters in output can better reflect the stochastic characteristics of the event. The temporal, spatial, and geometric properties of the breach have an impact on the peak breach discharge, and breach formation time is an important parameter that affects downstream inundation boundaries. In our study, each scenario responded differently to Monte Carlo simulation, but the impacts of the breach parameters were clearer in Scenario 1 than in other scenarios. The maximum discharge due to the higher EP case of 90% was 45% less compared to the lower EP case of 1%, and neither of the obtained EP discharges had a time of formation higher than the mean value. The results indicated that the maximum breach discharge is more sensitive to the breach width than the breach side slopes, which is in line with findings of Wahl (1998). Probability distribution and range of dam break parameters are crucial in the whole probabilistic framework, and having more certain judgments and information can significantly decrease the deviation of peak discharges among EP cases and impact resulting combinations of breach parameter sets. Moreover, the probabilistic approach enhances the precision of decisions in flood risk management and facilitates more accurate cost–benefit analyses in contrast to the traditional deterministic approach. Consequently, local government agencies can better prioritize actions in emergency and risk mitigation planning and allocate financial resources more effectively (Maranzoni et al. 2023).

In probabilistic dam breach analyses of rainy-day scenarios (i.e. Scenarios 2 and 3), the deviation ratios of peak discharges between lower and upper EP cases were much lower than those obtained in Scenario 1. This was due to the fact that the lower bound of peak discharges in rainy-day scenarios was defined by the inflow hydrographs. In addition to the geometric properties and time of formation of the breach, the outflow discharge was significantly influenced by the triggering water level of the failure. Simulations of Scenarios 2 and 3 showed that the peak discharge increased as the embankment withstood

the hydrostatic pressure over the crest level as much as possible. This behaviour may be specific to this particular embankment, as it could be caused by the size of the embankment and inadequate reservoir capacity compared to the inflow runoff. Although the initial reservoir level is found to have a significant impact on large-scale dams according to Rizzo et al. (2023), in the case of the small embankment mentioned above, the initial water level only caused minor delays in the breach hydrograph within the 24-h event of rainy-day scenarios.

The capacity of the embankment reservoir is a crucial factor that affects the peak discharge in dam breach simulations. In Scenario 3, the maximum discharge was obtained from the inflow hydrograph that was routed through the reservoir, and it was the highest among the various simulation results. Interestingly, some of the dam break simulations in Scenario 3 showed a decrease in the peak discharge that can be obtained from the reservoir routing. This was because the size of the embankment dam acts as a limiting factor, preventing the dam break progression from becoming more severe and causing the inflow hydrograph to become the dominant driving factor. In the specific case of this study, where the inflow is considerably higher than the reservoir capacity, the small size of the dam and the absence of overtopping protection in the embankment are advantageous factors in terms of mitigating the extent of flood damage experienced downstream.

Hydrodynamic flood models commonly employ Manning's roughness coefficients for floodplains based on historical flood events. However, the lack of data and natural spatial variability in dam breach flooding presents challenges (Rizzo et al. 2023). To mitigate spatial variability issues, this study utilized a high-resolution roughness layer with 10 m resolution and conducted a calibration process to match empirical data. Unfortunately, neither the calibration process nor the storms observed were of sufficient magnitude to provide a clear understanding of the roughness coefficient for floodplains that are likely to have a higher coefficient. Sensitivity analysis is a commonly used approach to evaluate roughness uncertainty (e.g. Sarchani and Koutroulis 2022), but this approach was not employed in this study due to the number of simulations required and the representational power of the manually verified roughness map. Additionally, the buildings defined as impermeable obstructions added restrictions, but for instance, a specific roughness coefficient was assigned to the roads for overcoming such these limitations.

A consistent finding across all scenarios is the occurrence of high velocities at hydraulic structure sites, contracted channels, road cover, and areas between structures that are geometrically aligned parallel to the flow direction. These velocities notably decrease as the frequency of high-resistance obstructions increases, which aligns with expectations in real flood scenarios. In terms of potential impact on loss of life, Scenario 1 emerged as a critical scenario due to the lack of sufficient time for alerting and implementing evacuation plans, especially considering the absence of a monitoring plan. On the other hand, Scenario 3 was the most severe scenario across various evaluation aspects, even in the higher EP cases. In any EP case of Scenario 3, it was likely that more than six structures would be affected to the highest degree possible during a potential event. This conclusion can also be extended to include Scenario 2 for all overtopping failure scenarios. As noted by Bharath et al. (2021), overtopping failure was shown to be more dangerous than failure due to piping, which aligns with the flood hazard results of this study.

While the peak discharges of the lower EP cases in Scenario 2 were comparable to or even greater than those of the higher EP cases in Scenario 3, none of the resulting inundated areas in Scenario 2 were larger than those in Scenario 3. This observation suggests that the propagation area of the flood is not solely determined by the peak discharge, but also influenced by other factors, such as the volume of runoff and the shape of the hydrograph. This inference can be extended to the assessment of flood hazards as well. Besides,

since the probabilistic dam breach analysis involves a series of assumptions from the initiation to the completion of the breach process, variations in dam breach and rainfall–runoff model parameters can also lead to different inflow hydrographs and peak discharges corresponding to different EPs. Additionally, the choice of rainfall distribution is a critical consideration, as a more optimistic distribution can lead to lower peak discharges resulting from rainfall–runoff simulation.

The utilization of a high-resolution DEM with a resolution of 2.5 m contributed significantly to the production of more reliable flood inundation and hazard maps. Psomiadis et al. (2021) also illustrated that employing a detailed terrain model, such as a digital surface model instead of a DEM, can better represent surface relief and natural obstacles like vegetation and buildings, thereby improving the precision of hydraulic simulation results. Furthermore, while a higher resolution terrain model could be employed, this would entail a significant increase in the simulation time beyond the current computation time of approximately 15 h for an average simulation, necessary to satisfy the Courant number condition. To ensure the stability of the model and the accuracy of the results, varying computation intervals were implemented in the models. Herein, the computation interval was regulated through the Courant number, which was limited to a maximum of 1 at any location within the computational mesh. Moreover, the appropriate grid cell size was chosen proportionally to the simulation time step to satisfy the Courant number condition and accurately capture all terrain features.

5 Conclusion

The objective of this study is to utilize a probabilistic modeling approach to evaluate the potential consequences of Kanlikoy Dam failure in the Nicosia district, Cyprus. The main focus is to identify the regions downstream of the dam that are susceptible to flooding. To achieve this, flood inundation and flood hazard maps were developed for three realistic scenarios, considering four different cases of exceedance probabilities. The methodology involved constructing hydrologic models to generate hydrographs corresponding to different scenarios. These hydrograph outputs were then utilized as inflows to the hydraulic models, which incorporated dam breach hydrographs. By integrating these components, the flood hazard levels in the study area were determined and assessed in detail.

In the hydrologic analysis, the annual maximum rainfall with a 100-year return period was determined through frequency analysis for Scenario 2, while the probable maximum precipitation was calculated using an envelope curve of frequency factor based on data from 36 different meteorological stations of the AMRS for Scenario 3. Subsequently, the HEC-HMS model of the dam catchment was employed to simulate the rainfall–runoff processes and generate hydrographs for the scenarios. Therefore, in addition to Scenario 1, which simulates piping failure without rainfall, the contributions of these hydrographs to the dam failure mechanism could be evaluated in Scenarios 2 and 3.

Probabilistic modeling using the McBreach software was employed to analyze potential dam breach scenarios, which generated different dam breach hydrographs. To simulate the propagation of flood waves resulting from these failure hydrographs, 2D HEC-RAS models based on a high-resolution DEM with the cell size of 2.5 m were utilized for hydrodynamic routing. To account for uncertainty in the dam breach hydrograph, two breach parameters for piping failure were calculated deterministically, while probability distributions were applied to the remaining six breach parameters. Additionally, five out of the six breach

parameters for overtopping failure were randomly sampled using probability distributions, while one parameter was deterministically defined. Then, the probabilistic analyses of breach hydrographs were conducted using a Monte Carlo method for each scenario.

The four hydrographs, representing the exceedance probabilities of 90%, 50%, 10%, and 1% for each scenario, were utilized as input for HEC-RAS models, and the resulting 2D hydraulic simulations were evaluated based on maximum depth, maximum velocity, and flood hazard levels. The downstream area was divided into five flood prone regions, enabling a detailed quantitative analysis of inundated areas, flooded roads, and structures at risk. The most critical flood hazard level of H6 primarily encompassed the main creek and the surrounding floodplain. However, Scenario 3 emerged as the most destructive, with H5 and H6 flood hazard zones dominating the entire inundated area. The findings demonstrated that as the scenarios became more severe, the hazard levels became increasingly critical, extending towards the settlements. In this context, local authorities must take action, particularly to mitigate risks in high hazard zones and provide safe evacuation plans to redirect individuals to areas with low flood hazard risk levels. Additionally, evacuation routes should be designed to avoid using bridges to enter emergency assembly locations since flooding significantly impacts hydraulic structures.

The results also demonstrated that in each scenario, the current and ongoing residential construction is at risk of being severely impacted by flooding. The existing flood measurements and open channels are inadequate to withstand the severe flood flows. With the expected increase in rainfall extremes due to climate change particularly in the Mediterranean region, the likelihood of flash flood events is anticipated to become more frequent and intense in the near future. Therefore, a monitoring system consisting of piezometers installed on the embankment body to detect pore water pressures that might indicate the risk of piping can be installed on the Kanlikoy Dam embankment. Additionally, local authorities should adopt an evacuation plan with synchronized early warning systems.

Author contributions All authors contributed to the study conception and design, to the analysis of the results and to the writing of the manuscript. Hydraulic and hydrologic models were developed by Atilla Onat Türkel.

Funding Open access funding provided by the Scientific and Technological Research Council of Türkiye (TÜBİTAK). No funding was received to assist with the preparation of this manuscript.

Declarations

Conflict of interests The authors have no relevant financial or non-financial interests to disclose.

Data availability Some or all data, models, or code generated or used during the study are proprietary or confidential in nature and may only be provided with restrictions.

Open Access This article is licensed under a Creative Commons Attribution 4.0 International License, which permits use, sharing, adaptation, distribution and reproduction in any medium or format, as long as you give appropriate credit to the original author(s) and the source, provide a link to the Creative Commons licence, and indicate if changes were made. The images or other third party material in this article are included in the article's Creative Commons licence, unless indicated otherwise in a credit line to the material. If material is not included in the article's Creative Commons licence and your intended use is not permitted by statutory regulation or exceeds the permitted use, you will need to obtain permission directly from the copyright holder. To view a copy of this licence, visit <http://creativecommons.org/licenses/by/4.0/>.

References

- Ahmad S, Simonovic SP (1999) Comparison of one-dimensional and two-dimensional hydrodynamic modeling approaches for Red River Basin. Report to the International Joint Commission-Red River Basin Task Force, Ottawa, Washington, pp 1–51
- Alcrudo F, Mulet J (2007) Description of the Tous Dam break case study (Spain). *J Hydraul Res* 45(1):45–57. <https://doi.org/10.1080/00221686.2007.9521832>
- Antzoulatos G, Kouloglou I-O, Bakratsas M, Moutzidou A, Gialampoukidis I, Karakostas A, Lombardo F, Fiorin R, Norbiato D, Ferri M, Symeonidis A, Vrochidis S, Kompatsiaris I (2022) Flood hazard and risk mapping by applying an explainable machine learning framework using satellite imagery and GIS Data. *Sustain* 14(6):3251. <https://doi.org/10.3390/su14063251>
- ASCE/EWRI Task Committee on Dam/Levee Breaching (2011) Earthen embankment breaching. *J Hydraul Eng* 137(12):1549–1564. [https://doi.org/10.1061/\(ASCE\)HY.1943-7900.0000498](https://doi.org/10.1061/(ASCE)HY.1943-7900.0000498)
- ASDSO (2023) Dam failures and incidents. Association of State Dam Safety Officials. <https://www.damsafety.org/incidents>. Accessed 8 Jan 2023
- Basheer T, Wayayok A, Yusuf B, Rowshon M (2017) Dam breach parameters and their influence on flood hydrographs for Mosul dam. *J Eng Sci Technol* 12:2896–2908
- Bello AAD, Argungu AS, Dinki ATS, Yahaya A, Sulaiman K, Salaudeen A, Abdullahi N (2024) Dam break study and its flood risk in Gurara watershed-Nigeria under varied spatio-temporal conditions by integrating HSPF and HEC-RAS models. *Environ Earth Sci* 83(4):136
- Bellos V, Tsakiris VK, Kopsiaftis G, Tsakiris G (2020) Propagating dam breach parametric uncertainty in a river reach using the HEC-RAS Software. *Hydrol* 7:72. <https://doi.org/10.3390/hydrology7040072>
- Bharath A, Shivapur V, Hiremath CG, Maddamsetty R (2021) Dam break analysis using HEC-RAS and HEC-GeoRAS: A case study of Hidkal dam, Karnataka state. *India Environ Chall* 5:100401. <https://doi.org/10.1016/j.envc.2021.100401>
- Bilali AE, Taleb I, Nafii A, Taleb A (2022) A practical probabilistic approach for simulating life loss in an urban area associated with a dam-break flood. *Int J Disaster Risk Sci* 76:103011
- Boucefiane A, Meddi M (2022) Estimation of the probable maximum precipitation (PMP) in the Cheliff semi-arid region (Algeria). *Meteorol Atmos Phys* 134(2):34. <https://doi.org/10.1007/s00703-022-00864-y>
- Brunner G (2014) Using HEC-RAS for Dam Break Studies. Report TD-39. US Army Corps of Hydrologic Engineering Center, Davis, CA
- Brunner GW (2020) United States., Army., Corps of Engineers., Institute for Water Resources (U.S.), Hydrologic Engineering Center (U.S.). HEC-RAS river analysis system: Hydraulic reference manual. US Army Corps of Engineers, Institute for Water Resources, Hydrologic Engineering Center
- Faeh R (2007) Numerical modeling of breach erosion of River Embankments. *J Hydraul Eng* 133(9):1000–1009. [https://doi.org/10.1061/\(ASCE\)0733-9429\(2007\)133:9\(1000\)](https://doi.org/10.1061/(ASCE)0733-9429(2007)133:9(1000))
- FEMA (Federal Emergency Management Agency) (2013) Federal guidelines for inundation mapping of flood risks associated with dam incidents and failures, 1st edn, FEMA P-946, Washington DC
- FERC (Federal Energy Regulatory Commission) (1988) Engineering Guidelines for the Evaluation of Hydropower Projects, revised in 1993, USA
- Fread DL (1988) Breach: an erosion model for earthen dam failures. National Weather Service, National Oceanic and Atmospheric Administration, Silver Springs, MD
- Froehlich DC (2008) Embankment dam breach parameters and their uncertainties. *J Hydraul Eng* 134(12):1708–1721. [https://doi.org/10.1061/\(ASCE\)0733-9429\(2008\)134:12\(1708\)](https://doi.org/10.1061/(ASCE)0733-9429(2008)134:12(1708))
- Froehlich DC (2016) Predicting peak discharge from gradually breached embankment Dam. *J Hydrol Eng* 21:04016041. [https://doi.org/10.1061/\(ASCE\)HE.1943-5584.0001424](https://doi.org/10.1061/(ASCE)HE.1943-5584.0001424)
- Goodell C, Raeburn R, Karki A, Johnson D, Monk S, Lee A (2018) Probabilistic dam breach modeling using HEC-RAS and Mcbreach
- Goodell C (2019) McBreach, probabilistic dam breach modeling user's manual, Version 5.0.7, June 2019. Portland, Oregon: Kleinschmidt Associates
- Guido BI, Popescu I, Samadi V, Bhattacharya B (2023) An integrated modelling approach to evaluate the impacts of nature-based solutions of flood mitigation across a small watershed in the southeast United States. *Nat Hazards Earth Syst Sci* 2023:1–30
- Hadjinicolaou P, Giannakopoulos C, Zerefos C, Lange MA, Pashiardis S, Lelieveld J (2010) Mid-21st century climate and weather extremes in Cyprus as projected by six regional climate models. *Reg Environ Change* 11(3):441–457. <https://doi.org/10.1007/s10113-010-0153-1>
- Hagos YG, Andualem TG, Yibeltal M, Mengie MA (2022) Flood hazard assessment and mapping using GIS integrated with multi-criteria decision analysis in upper Awash River basin. *Ethiopia Appl Water Sci* 12(7):148. <https://doi.org/10.1007/s13201-022-01674-8>

- Haltas I, Elçi S, Tayfur G (2016) Numerical simulation of flood wave propagation in two-dimensions in densely populated urban areas due to Dam Break. *Water Resour Manage* 30(15):5699–5721. <https://doi.org/10.1007/s11269-016-1344-4>
- Hershfield DM (1965) Method for estimating probable maximum rainfall. *J Am Water Works Assoc* 57(8):965–972. <https://doi.org/10.1002/j.1551-8833.1965.tb01486.x>
- Jibhakate SM, Timbadiya P, Patel PL (2023) Flood hazard assessment for the coastal urban floodplain using 1D/2D coupled hydrodynamic model. *Nat Hazards* 116(2):1557–1590
- Konteatis CAC (1974) Dams of cyprus. Water Development Department, Ministry of Agriculture and Natural Resources, Nicosia Cyprus
- MacDonald TC, Langridge-Monopolis J (1984) Breaching characteristics of dam failures. *J Hydraul Eng* 110(5):567–586. [https://doi.org/10.1061/\(ASCE\)0733-9429\(1984\)110:5\(567\)](https://doi.org/10.1061/(ASCE)0733-9429(1984)110:5(567))
- Mani P, Chatterjee C, Kumar R (2014) Flood hazard assessment with multiparameter approach derived from coupled 1D and 2D hydrodynamic flow model. *Nat Hazards* 70(2):1553–1574. <https://doi.org/10.1007/s11069-013-0891-8>
- Maranzoni A, D’Oria M, Rizzo C (2023) Probabilistic mapping of life loss due to dam-break flooding. *Nat Hazards* 120:2433–2460. <https://doi.org/10.1007/s11069-023-06285-3>
- Papaioannou G, Efstratiadis A, Vasiliades L, Loukas A, Papalexiou S, Koukouvinos A, Tsoukalas I, Kossieris P (2018) An operational method for flood directive implementation in ungauged urban areas. *Hydrol* 5(2):24. <https://doi.org/10.3390/hydrology5020024>
- Pasquier U, He Y, Hooton S, Goulden M, Hiscock KM (2019) An integrated 1D–2D hydraulic modelling approach to assess the sensitivity of a coastal region to compound flooding hazard under climate change. *Nat Hazards* 98(3):915–937. <https://doi.org/10.1007/s11069-018-3462-1>
- Pierce MW, Thornton CI, Abt SR (2010) Predicting peak outflow from breached embankment dams. *J Hydraul Eng* 15(5):338–349. [https://doi.org/10.1061/\(ASCE\)JHE.1943-5584.0000197](https://doi.org/10.1061/(ASCE)JHE.1943-5584.0000197)
- Piloti M, Maranzoni A, Tomirotti M, Valerio G (2011) 1923 Gleno Dam Break: case study and numerical modeling. *J Hydraul Eng* 137(4):480–492. [https://doi.org/10.1061/\(ASCE\)HY.1943-7900.0000327](https://doi.org/10.1061/(ASCE)HY.1943-7900.0000327)
- Ponce VM, Tsivoglou AJ (1981) Modeling gradual dam breaches. *J Hydr Div* 107(7):829–838. <https://doi.org/10.1061/JYCEAJ.0005694>
- Psomiadis E, Tomanis L, Kavvadias A, Soulis KX, Charizopoulos N, Michas S (2021) Potential dam breach analysis and flood wave risk assessment using HEC-RAS and remote sensing data: a multicriteria approach. *Water* 13(3):364
- QGIS Development Team (2020) QGIS Geographic Information System. Open Source Geospatial Foundation Project
- Rakhecha PR, Deshpande NR, Soman MK (1992) Probable maximum precipitation for a 2-day duration over the Indian Peninsula. *Theor Appl Climatol* 45(4):277–283. <https://doi.org/10.1007/BF00865518>
- Rizzo C, Maranzoni A, D’Oria M (2023) Probabilistic mapping and sensitivity assessment of dam-break flood hazard. *Hydrol Sci J* 1–19. <https://doi.org/10.1080/02626667.2023.2174026>
- Sarchani S, Koutroulis AG (2022) Probabilistic dam breach flood modeling: the case of Valsamiotis dam in Crete. *Nat Hazards* 114(2):1763–1814. <https://doi.org/10.1007/s11069-022-05446-0>
- SCS (1972) National Engineering Handbook, Section 4. Hydrology, Soil Conservation Service, USDA, U.S. Dept. of Agriculture, Washington
- Smith GP, Davey EK, Cox R (2014) WRL technical report. University of South Wales, Australia, Water Research Laboratory
- Solava S, Delatte N (2003) Lessons from the failure of the Teton Dam. *Forensic Engineering* (2003). American Society of Civil Engineers, San Diego, CA, pp 178–189
- Tien Bui D, Pradhan B, Nampak H, Bui Q-T, Tran Q-A, Nguyen Q-P (2016) Hybrid artificial intelligence approach based on neural fuzzy inference model and metaheuristic optimization for flood susceptibility modeling in a high-frequency tropical cyclone area using GIS. *J Hydrol* 540:317–330. <https://doi.org/10.1016/j.jhydrol.2016.06.027>
- Tsakiris G, Bellos V (2014) A numerical model for two-dimensional flood routing in complex terrains. *Water Resour Manage* 28(5):1277–1291. <https://doi.org/10.1007/s11269-014-0540-3>
- USACE (1980) Flood emergency plans. “Guidelines for corps dams” (version RD-13, June). California, pp 62
- USBR (United States Bureau of Reclamation) (1988) Downstream Hazard Classification Guidelines. ACER Technical Memorandum No. 11, Assistant Commissioner-Engineering and Research, Denver, Colorado 92
- Von Thun JL, Gillette DR (1990) Guidance on breach parameters. Denver, Colorado: U.S. Dept. of the Interior, Bureau of Reclamation

- Visser PJ (1998) Breach growth in Sand Dikes. Doctoral Thesis, TU Delft, retrieved from: <http://resolver.tudelft.nl/uuid:3721e23b-d34c-45a9-8b36-e5930462d8e2>
- Wahl TL (2004) Uncertainty of predictions of embankment dam breach parameters. *J Hydraul Eng* 130(5):389–397. [https://doi.org/10.1061/\(ASCE\)0733-9429\(2004\)130:5\(389\)](https://doi.org/10.1061/(ASCE)0733-9429(2004)130:5(389))
- Wahl TL (1998) Prediction of embankment dam breach parameters—a literature review and needs assessment. Dam Safety Report. DSO-98-004. US Department of the Interior, Bureau of Reclamation, Denver, CO
- Walder JS, O'Connor JE (1997) Methods for predicting peak discharge of floods caused by failure of natural and constructed earthen dams. *Water Resour Res* 33(10):2337–2348. <https://doi.org/10.1029/97WR01616>
- Wang Z, Bowles DS (2006) Three-dimensional non-cohesive earthen dam breach model. Part 1: theory and methodology. *Adv Water Resource* 29(10):1528–1545. <https://doi.org/10.1016/j.advwatres.2005.11.009>
- WMO (World Meteorological Organization). Manual on estimation of probable maximum precipitation (PMP), WMO-No. 1045, 259 pp
- Wright DB, Yu G, England JF (2020) Six decades of rainfall and flood frequency analysis using stochastic storm transposition: Review, progress, and prospects. *J Hydrol* 585:124816. <https://doi.org/10.1016/j.jhydrol.2020.124816>
- Xu Y, Zhang LM (2009) Breaching parameters for earth and Rockfill Dams. *J Geotech Geoenviron Eng* 135(12):1957–1970. [https://doi.org/10.1061/\(ASCE\)GT.1943-5606.0000162](https://doi.org/10.1061/(ASCE)GT.1943-5606.0000162)
- Yilmaz K, Darama Y, Oruc Y, Melek AB (2023) Assessment of flood hazards due to overtopping and piping in Dalaman Akköprü Dam, employing both shallow water flow and diffusive wave equations. *Nat Hazards* 117(1):979–1003
- Zaifoglu H, Akintug B, Yanmaz AM (2017) Quality control, homogeneity analysis, and trends of extreme precipitation indices in Northern Cyprus. *J Hydrol Eng* 22(12):05017024. [https://doi.org/10.1061/\(ASCE\)HE.1943-5584.0001589](https://doi.org/10.1061/(ASCE)HE.1943-5584.0001589)
- Zaifoglu H, Yanmaz AM, Akintug B (2019) Developing flood mitigation measures for the northern part of Nicosia. *Nat Hazards* 98(2):535–557. <https://doi.org/10.1007/s11069-019-03713-1>
- Zanaga D, Van De Kerchove R, De Keersmaecker W, Souverijns N, Brockmann C, Quast R, Wevers J, Grosu A, Paccini A, Vergnaud S, Cartus O, Santoro M, Fritz S, Georgieva I, Lesiv M, Carter S, Herold M, Li L, Tsendbazar N-E, Ramoino F, Arino O (2021) ESA WorldCover 10 m 2020 v100
- Zhang L, Peng M, Chang D, Xu Y (2016) Dam failure mechanisms and risk assessment, 1st edn. Wiley, Singapore

Publisher's Note Springer Nature remains neutral with regard to jurisdictional claims in published maps and institutional affiliations.